The Relationship between Boundary Layer Stability and Cloud Cover in the Post-Cold-Frontal Region

CATHERINE M. NAUD

Applied Physics and Applied Mathematics, Columbia University, and NASA GISS, New York, New York

JAMES F. BOOTH

Earth and Atmospheric Sciences, CUNY City College, New York, New York

ANTHONY D. DEL GENIO

NASA GISS, New York, New York

(Manuscript received 6 October 2015, in final form 10 August 2016)

ABSTRACT

Using NASA *Aqua* MODIS and AIRS data, the relationship between low-level cloud cover (cloud top below the 700-hPa level) and boundary layer stability is explored in post-cold-frontal conditions. A linear relationship is found between seasonal cloud cover and two separate measures of inversion strength, the lower-tropospheric stability (LTS) and the estimated inversion strength (EIS), for two specific regions in the North Atlantic and Pacific in quiescent and weakly subsiding conditions. The relationship barely changes when considering dynamically active and subsiding post-cold-frontal conditions for the same regions. To explore the generality of this result and increase sample size, cold-front-centered composites of cloud cover and stability are constructed. The Northern and Southern Hemisphere seasonal cloud cover and stability distributions in the post-cold-frontal regions are then compared. A fairly good correlation between cloud cover and EIS is found in both hemispheres across all seasons, suggesting that a linear relationship between cloud cover and inversion strength proposed for quiescent conditions exists also in more dynamically active subsiding post-cold-frontal conditions. However, for a given season and hemisphere, the correlation between cloud cover and EIS degrades in post-cold-frontal regions, especially in the Northern Hemisphere. At these scales, other large-scale factors tend to correlate better with cloud cover.

1. Introduction

In the past few years, a renewed interest in modeled representation of cloud cover in the midlatitudes has occurred, in part motivated by the work of Trenberth and Fasullo (2010), who found a systematic negative cloud-cover bias in most general circulation models (GCMs) over the southern oceans and suggested that the resulting excess absorption of shortwave radiation has implications for global climate sensitivity. Hwang and Frierson (2013) suggested that this shortwave bias is also the source of the widespread double intertropical convergence zone problem in GCMs.

Because the bias is most acute in regions dominated by extratropical cyclones, Bodas-Salcedo et al. (2014) examined phase 5 of the Coupled Model Intercomparison Project (CMIP5) models and found that most did not produce large enough cloud cover in the cold sector of cyclones. Naud et al. (2014) found a similar issue in the European Centre for Medium-Range Weather Forecasts (ECMWF) interim reanalysis (ERA-Interim; Dee et al. 2011) and in the NASA Modern-Era Retrospective Analysis for Research and Applications (MERRA; Rienecker et al. 2011). The cold sector of extratropical cyclones wraps around the cyclone center on the western side and on its equatorward edge contains the post-cold-frontal region. This region is dominated by subsidence and populated by

Denotes Open Access content.

Corresponding author address: Catherine M. Naud, Applied Physics and Applied Mathematics, Columbia University, 2880 Broadway, New York, NY 10025.
E-mail: cn2140@columbia.edu

DOI: 10.1175/JCLI-D-15-0700.1

low-level, often broken, clouds (e.g., Lau and Crane 1997; Norris and Iacobellis 2005; Naud et al. 2014, 2015). Low-level clouds—that is, cumulus, stratocumulus, stratus, fractocumulus, and fractostratus in the nomenclature of the ground observers (e.g., Klein and Hartmann 1993, hereafter KH93)—are notoriously difficult to simulate (e.g., Tselioudis and Jakob 2002; Field et al. 2011; Govekar et al. 2014), as they involve parameterizations of the boundary layer, convection, and stratiform clouds.

In an effort to document the environmental controls on low-level stratiform cloud amount, KH93 found a good correlation in seasonal and regional mean cloud amount with a measure of lower-tropospheric stability (LTS; defined as the difference in potential temperature between 700 hPa and the surface). As a consequence, some models have used this relationship in the parameterization of boundary layer clouds (e.g., Rasch and Kristjánnson 1998; Köhler et al. 2011). However, this correlation was tested and intended for subtropical regions, and the two midlatitude regions KH93 examined displayed larger cloud cover for a given LTS. Wood and Bretherton (2006, hereafter WB06) argued that using the KH93 LTS-based relationship as a parameterization might be inappropriate for simulating climate changes in low clouds. They proposed a refined measure of boundary layer stability, the estimated inversion strength (EIS), which corrects LTS by taking into account the moist-adiabatic potential temperature gradient at 850 hPa. They found a strong correlation between cloud amount and EIS not only for the subtropics but also for undisturbed and weakly subsiding regions in the tropics and midlatitudes. Both studies used seasonal and regional averages, in conditions of undisturbed and weak subsidence. Thus, it is unclear how good the correlation between cloud amount and EIS might be in post-cold-frontal regions where subsidence can be stronger and where dynamical conditions are highly disturbed.

In this paper, we test whether the linear relationship between cloud amount and both LTS and EIS across seasons still holds in oceanic post-cold-frontal regions. We explore these two questions: 1) does this region of cyclones display a strong correlation between boundary layer stability and cloud amount, and 2) does this relation differ between the hemispheres? To tackle this problem, we use NASA *Aqua* Moderate Resolution Imaging Spectroradiometer (MODIS; Salomonson et al. 1989) cloud cover (CC) and Atmospheric Infrared Sounder/Advanced Microwave Sounding Unit (AIRS/AMSU, simply referred to as AIRS hereafter; Chahine et al. 2006) temperature profiles. We compare the relationship between cloud cover and both LTS/EIS in the same midlatitude regions as tested in KH93 and WB06 and then explore whether it changes under post-cold-frontal conditions. The observations are composited for the entire extratropical oceanic region in a cold-front-centered grid separately for each season and hemisphere, so we can verify the generality of the relationship between cloud cover and stability.

2. Data and method

Our study focuses on the 20°–60°N–S oceans and spans the time period from November 2006 to September 2007.

a. Cloud-cover datasets

MODIS cloud properties are available in 5-min granules along the *Aqua* platform orbits, and here we use the MYD06 files of the collection 5.1. The size of 12 months of data is ~1 terabyte (TB, for November 2006 to October 2007) and even larger for collection 6; therefore, we focus here on a single year. Naud et al. (2013) demonstrated that one extended cold season provides enough sampling to explore extratropical cyclone cloud properties. Since we are interested in scenes populated by low-level clouds, 5-km-resolution MODIS cloud-top pressures (Menzel et al. 2008) are extracted and pixels are selected if the cloud-top pressure is greater than 700 hPa (or the pixel is clear). Sometimes low clouds under strong inversions are assigned a cloud-top pressure that is too low (Garay et al. 2008; Holz et al. 2008). This was found to occur mostly in oceanic regions frequently covered with stratocumulus clouds, equally in winter and summer (Holz et al. 2008). This can cause a 5-km pixel to be erroneously discarded from our study.

There are two cloud-cover retrievals in the files: A 5-km resolution product available day and night based on the 1-km cloud mask (Ackerman et al. 2008) with a tendency to be clear conservative (i.e., if a 1-km pixel is partly filled with cloud, it is deemed cloudy). Another cloud-cover product is available that is in contrast cloud conservative for use in microphysical property retrieval, available at 1-km resolution only during the daytime (Platnick et al. 2003). This product categorizes a 1-km pixel as cloudy only if it is fully cloud covered. For convenience, we calculate a new cloud-conservative cloud cover by averaging the latter over a 5 km × 5 km zone collocated with the cloud-top pressure and clear-conservative cloud cover. The difference between the two retrievals (clear conservative minus cloud conservative) is used here as an indicator of the ''brokenness'' of the clouds (i.e., the greater its magnitude, the greater the heterogeneity of the scene).

We refer to this quantity as the frequency of partly filled pixels.

b. Observation-derived estimated inversion strength

The estimated inversion strength (WB06) parameter is defined as follows:

$$\mathrm{EIS} = \mathrm{LTS} - \Gamma_m^{850}(Z_{700} - \mathrm{LCL}), \quad (1)$$

where LTS is the lower-tropospheric stability parameter of KH93—that is, the difference in potential temperature between 700 hPa and the surface (LTS = $\theta_{700} - \theta_{\mathrm{surf}}$). The quantity Γ_m^{850} is the moist-adiabatic potential temperature gradient at 850 hPa; Z_{700} is the altitude of the 700-hPa level and LCL is the lifting condensation level.

The AIRS level 2 version 5 standard and support product files provide profiles of temperature and surface air temperature (e.g., Susskind et al. 2003), along with National Centers for Environmental Prediction Global Forecast System (NCEP GFS) interpolated surface pressure. The quality of the AIRS profiles degrades as the signal from the surface becomes attenuated by clouds in a 45-km-radius region. This can happen in situations of low contrast (e.g., uniform thin cirrus or fog), large cloud fractions, large water content, or very cold surface (J. Blaisdell 2015, personal communication). Consequently, we use a flag that indicates the pressure level below which the quality of the retrievals is poor. This causes LTS and EIS to sometimes be unavailable below 700 hPa. According to Yue et al. (2011), who use an even stricter requirement for their AIRS profile quality assessment in marine boundary layer clouds regions, up to 90% of AIRS retrievals can be kept for cloud cover less than 0.6 and 60%–70% for cloud cover of 0.6 to 0.9 but less than 20% in overcast situations, such as extensive marine stratocumulus decks. The profiles include retrievals of temperature and geopotential height at 700 hPa, and surface air temperatures are also available.

To calculate LTS, we use AIRS 700-hPa temperature and AIRS surface air temperature. For LCL, we use the same equation as in Yue et al. (2011): LCL = 125($T - T_d$), where T is the surface temperature and T_d is the dewpoint temperature at the surface assuming (as in WB06) a relative humidity over the oceans of 80%. We do not have surface relative humidity data; instead we use AIRS retrievals at 1000 hPa of specific humidity and saturation specific humidity. We also extract ERA-Interim 1000-hPa relative humidity. With both products, we verified that the average relative humidity is close to 80% in undisturbed weakly subsiding and post-cold-frontal conditions. For Γ_m^{850}, we use the formula given in WB06 [their Eq. (5)], for which we need surface air and 700-hPa temperatures and the saturation specific humidity at 850 hPa, which we approximate with an empirical formula proposed by Bolton (1980) based on temperature.

c. Cold front detection

To identify the post-cold-frontal regions, we first locate extratropical cyclones using the Modeling, Analysis, and Prediction (MAP) Program Climatology of Midlatitude Storminess (MCMS; Bauer and Del Genio 2006; Bauer et al. 2016) database. Then we locate the cold fronts using the 0.5° × 0.667° 6-hourly MERRA outputs. For this, two objective methods exist: one based on temperature gradients (Hewson 1998) and the other on wind changes (Simmonds et al. 2012).

Hewson (1998) uses the potential temperature field at 1 km above the surface and isolates areas where the temperature gradient is abrupt enough to mark the location of a warm or cold front. Simmonds et al. (2012) rely on the temporal change in 850-hPa meridional wind direction and strength when a cold front passes through a grid cell between two consecutive (6 hourly) time steps. Schemm et al. (2015) find a tendency for the Hewson (1998) method to succeed in detecting fronts more often if the conditions are strongly baroclinic, whereas the success rate of the Simmonds et al. (2012) method is larger in situations of relatively weaker baroclinicity. Because they are complementary, we use a combination of both methods, as follows (see also Fig. 1):

1) Using the MCMS cyclone locations database, we define an area centered on a low pressure center that extends ±40° north–south and east–west. In this region, we extract MERRA temperature and geopotential heights to obtain a regional gridded potential temperature field at 1-km altitude and calculate the difference in direction and magnitude of the 850-hPa meridional wind between the time of cyclone detection and 6 h prior.
2) We calculate the spatial rate of change of the potential temperature gradient and look for the MERRA grid cells where the along-vector divergence of this quantity is zero (Hewson 1998; Naud et al. 2010). We apply the same masking tests as Hewson (1998) to only keep the grid cells with a strong enough front. Finally, we distinguish the cold from the warm front using the sign of the geostrophic thermal advection (negative for cold fronts). The result is a mask that indicates the grid cells containing a cold front.
3) We then use the meridional wind time difference field and mark as cold front locations the grid cells where the wind changes sign and the difference in magnitude is at least 2 m s^{-1}. The result is a second

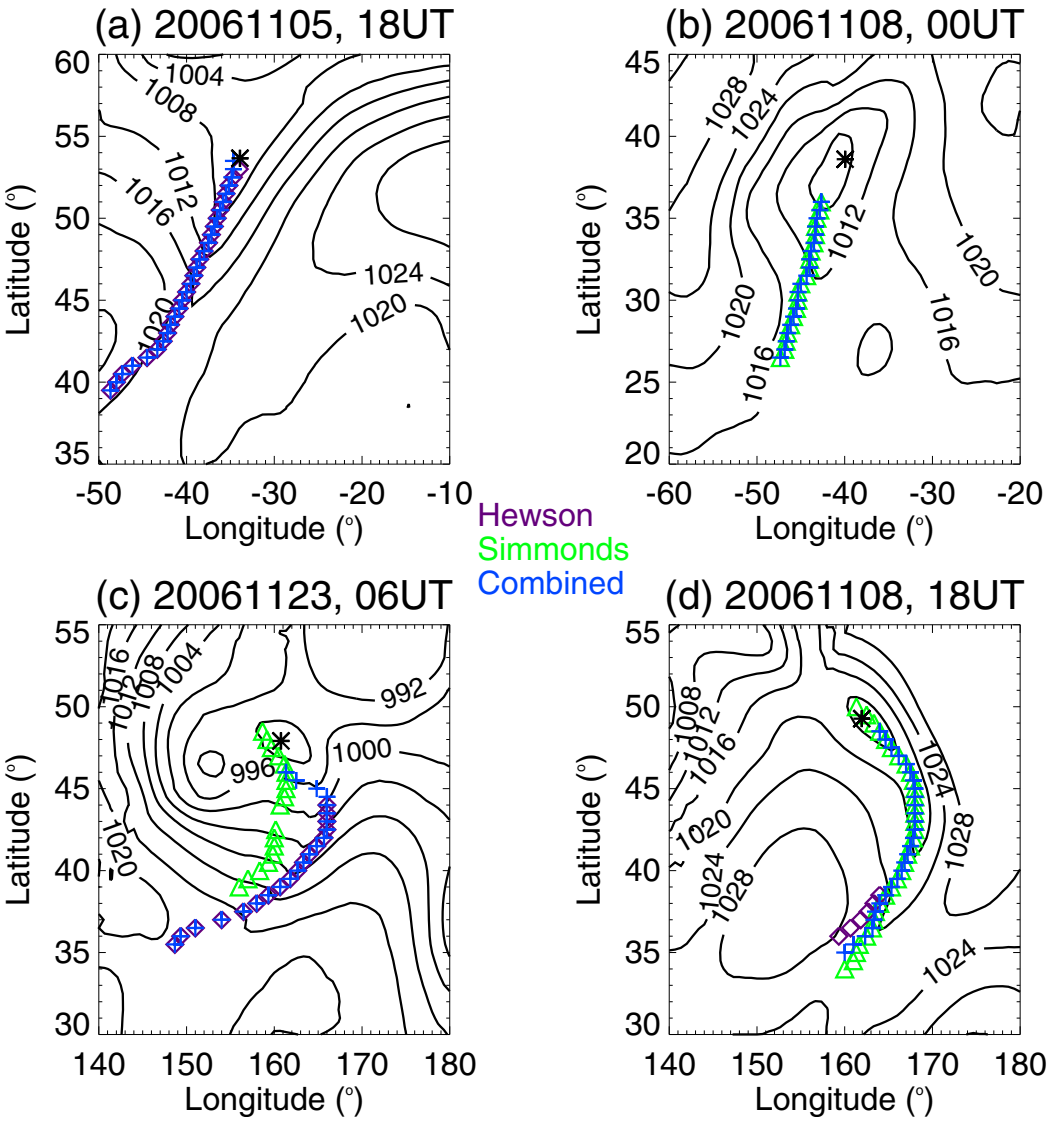

FIG. 1. Examples of automated cold front detection for four Northern Hemisphere ocean cold season cyclones that occurred on (a) 1800 UTC 5 Nov 2006, (b) 0000 UTC 8 Nov 2006, (c) 0600 UTC 23 Nov 2006, and (d) 1800 UTC 8 Nov 2006. The purple squares mark the detections with the Hewson (1998) method, the green triangles mark detection with Simmonds et al. (2012), and the blue plus signs show the cold front detected by combining the two methods (see text). The solid contours give the MERRA sea level pressure, and the black asterisk indicates the location of the cyclone low pressure center.

gridded mask that indicates the grid cells where the Simmonds et al. (2012) method finds cold fronts.

4) Regardless of whether one or both methods are successful at detecting cold frontal locations, we construct a third gridded mask that contains all locations flagged by either method. Using this combined gridded mask, we then apply a series of tests. First we apply a cluster detection routine to separate groups of neighboring grid cells into distinct candidate cold fronts. These clusters are not necessarily clear linear boundaries, so we apply the same criterion as Simmonds et al. (2012); the latitudes of the points within each cluster are sorted, and for each latitude we only keep the easternmost point. If some of the resulting clusters (i.e., candidate cold fronts) contain fewer than three points, they are rejected. We then apply to the remaining candidates a series of tests that are to some extent arbitrary but were designed based on the visual examination of multiple cases: 1) the mean latitude of each candidate front should be between 20° and 70°N–S, 2) the mean distance between the candidate front and the parent low pressure

center should be within 15° latitude and 7.5° longitude to prevent keeping a cold front that is in fact associated with another cyclone, and 3) the mean latitude of the candidate cold front should be equatorward of the low. If more than one candidate obeys all the criteria, they are considered to be all part of the same cold front and combined into one (possibly disjointed) candidate cold front. Finally, as in Simmonds et al. (2012), a Hanning smoothing function is applied to the resulting latitude–longitude vector.

Figure 1 summarizes the different possible outcomes. Figure 1a shows a cold front detected by the Hewson (1998) technique; in this situation the Simmonds et al. (2012) technique could not detect a cold front. Figure 1b shows an example for which only the Simmonds et al. (2012) technique was successful. Figure 1c illustrates a situation where both techniques were successful but disagreed on the location of the cold front. In this case, the processing of the combined gridded mask gave a cold front that was mostly detected with the Hewson (1998) technique, which in this case looks more realistic as it better follows the kink in the pressure contours. Finally, a large number of cases show that both methods indicate candidate locations that are very close to one another, as illustrated in Fig. 1d.

Over nearly 4500 cyclones, we found that a cold front could be detected about 85% of the time, with the Simmonds et al. (2012) technique identifying a cold front in 74% of all cyclones and Hewson (1998) in 52%. In about 41% of all cases both methods were successful. The success rate for detection degrades in summer compared to winter cyclones, especially for the Hewson (1998) technique, which performs better in high baroclinicity events (Schemm et al. 2015).

3. Relationship between cloud cover and LTS/EIS in two midlatitude oceanic regions

Before investigating post-cold-frontal regions, we evaluate how the relations explored in KH93 and WB06 look for our datasets. In both prior studies, monthly cloud cover was obtained from the Warren et al. (1988) cloud atlas and the stability measures were obtained from ship-based observations and reanalysis. In our case, we use satellite datasets, which have some limitations:

1) Cloud type is unknown and so we cannot exclude cumulus fields, as is done in KH93 and WB06. This might cause errors in MODIS cloud cover.
2) We expect the clear-conservative cloud cover to overestimate, and the cloud-conservative cloud cover to underestimate, the real cloud cover.
3) MODIS cloud-top pressure can be underestimated when a strong inversion occurs, causing these situations to be arbitrarily excluded by our fixed 700-hPa cloud-top threshold.
4) AIRS retrievals become unreliable as cloud cover becomes too large for the surface signal to be available.

To explore the implication of these issues for the relationship between MODIS cloud cover and AIRS estimates of LTS and EIS, we calculate the seasonal means of these three quantities in the two midlatitude regions KH93 and WB06 investigated: the North Atlantic (50°–60°N and 45°–35°W) and the North Pacific (40°–50°N and 170°–180°E). We then compare the results with those of KH93 and WB06 in quiescent conditions and then in post-cold-frontal conditions. MODIS and AIRS observations are collocated and coincident, but we allow in our averages instances when only one of the two instruments actually provides a retrieval. We verified that this does not affect our conclusions as discussed in section 3b below.

a. *Evaluation of the usability of the satellite observations*

When we calculate the seasonal mean of AIRS LTS and EIS, we impose a constraint as was done by WB06; near-coincident and collocated ERA-Interim vertical velocity must indicate weak subsidence (0.2–0.8 cm s^{-1}). To estimate the impact of not having AIRS retrievals in overcast scenes, we also calculate LTS and EIS using ERA-Interim output. Table 1 gives the seasonal average of EIS and LTS for the two datasets. The mean AIRS LTS and EIS values agree remarkably well with ERA-Interim estimates, although AIRS LTS (and EIS) tend to often be slightly lower than ERA-Interim's estimates. This is expected as scenes with no AIRS retrievals are expected to be the overcast, strong inversion cases. However, the impact of these scenes tends to be similar across seasons, and the difference is very small relative to the standard deviations and the actual values of the parameters. Overall the agreement for all seasons between the AIRS LTS and EIS values and the KH93 and WB06 estimates is good despite AIRS limitations. And, of importance for our study, we find a similar change in inversion strength across seasons. In view of these results, we trust that AIRS estimates of inversion strength can be used in our study.

When we calculate the MODIS seasonal mean cloud cover, we impose that the cloud-top pressure for cloudy pixels is greater than 700 hPa. For comparison against MODIS, we use the 1954–97 low-level cloud seasonal average from the Warren et al. (1988) cloud atlas available on the University of Washington website (to mimic

TABLE 1. Seasonal averages and one standard deviation of LTS and EIS estimated using ERA-Interim and AIRS in weakly subsiding conditions and of cloud cover (CC) obtained from MODIS clear-conservative and cloud-conservative retrievals and using the online tool of the Warren et al. (1988) cloud atlas for the North Atlantic (NA; 50–60°N, 35°–45°W) and the North Pacific (NP; 40°–50°N, 170°–180°E) regions of KH93. [Source for the Warren et al. (1988) cloud atlas estimates: http://www.atmos.washington.edu/CloudMap.]

	AIRS		ERAI		MODIS		Warren et al. (1988) cloud atlas
Season–region	LTS (K)	EIS (K)	LTS (K)	EIS (K)	Clear-conservative CC (%)	Cloud-conservative CC (%)	Low-level CC (%)
DJF–NA	10.8 ± 4.5	3.7 ± 3.7	10.1 ± 4.4	3.3 ± 3.8	85 ± 26	69 ± 40	74
MAM–NA	12.8 ± 5.0	5.1 ± 3.9	12.3 ± 4.9	5.0 ± 3.8	82 ± 31	62 ± 44	73
JJA–NA	18.7 ± 4.2	7.9 ± 3.7	18.1 ± 3.8	7.1 ± 3.6	86 ± 31	76 ± 40	77
SON–NA	13.8 ± 5.3	4.9 ± 4.1	13.0 ± 5.0	4.2 ± 3.9	79 ± 32	60 ± 43	72
DJF–NP	7.4 ± 3.0	1.0 ± 2.9	7.5 ± 4.0	0.7 ± 3.2	76 ± 32	50 ± 44	71
MAM–NP	15.1 ± 4.7	7.1 ± 3.7	16.6 ± 5.0	6.9 ± 4.0	84 ± 31	67 ± 43	77
JJA–NP	22.4 ± 3.0	10.5 ± 3.0	21.2 ± 3.5	9.6 ± 3.0	90 ± 26	86 ± 32	87
SON–NP	15.9 ± 4.7	5.6 ± 3.6	15.6 ± 4.8	5.0 ± 3.9	77 ± 34	60 ± 45	73

MODIS sampling, the averages include all low-level clouds, not just stratus or stratocumulus types). Table 1 gives the seasonal means of cloud cover. As expected, MODIS clear-conservative cloud cover is larger than the ground observers' estimates while MODIS cloud-conservative cloud cover is the lowest of the three. For the North Atlantic region, the variation across seasons is the same using either the definition of MODIS cloud cover or the ground-observers' definition; there is a relative minimum during the intermediate seasons compared to winter, and the maximum occurs in summer. This is different from the estimates in both KH93 and WB06 and from the North Pacific region, where cloud cover during the intermediate seasons was slightly larger than the winter values. Because our analysis includes all low-level cloud from the cloud atlas, the difference in seasonality, as compared with KH93 and WB06, suggests that the frequency of occurrence of the cumulus clouds that are not included in the previous studies changes with season for this location. The North Atlantic region is farther north than that of North Pacific and closer to land. We suspect that this proximity to possibly snow-covered land might influence the cloud cover and affects its correlation to local boundary layer structure.

Finally, we tested if the mean cloud-cover averages were sensitive to the 700-hPa threshold. We find that when we change the threshold to 600 hPa, cloud cover increases, which is expected if by doing so we include more of the strong inversion cases for which MODIS underestimates cloud-top pressure. However, this increase occurs for all seasons and using the new threshold does not change the seasonal variations.

North Atlantic and North Pacific seasonal averages of cloud-conservative MODIS cloud cover are plotted against AIRS LTS and EIS in Figs. 2a and 2b, respectively. For both LTS and EIS and the two regions, the correlation coefficients are large and the linear fit is a good approximation of the relationship.

In WB06, the linear fit between cloud cover and EIS has a slope of $0.06\,K^{-1}$ when all sites (including a large number of subtropical locations) and all seasons are included. However, when only the North Atlantic midlatitude location is considered in WB06 (their Fig. 6b), the slope might be closer to $0.03\,K^{-1}$. Using the same subtropical and midlatitude regions as in WB06 but with AIRS estimates of EIS and *CloudSat–CALIPSO* cloud cover, Yue et al. (2011) found a slope of $\sim 0.03\,K^{-1}$. Here, using the cloud-conservative definition of cloud cover and AIRS, the slope is also approximately $0.03\,K^{-1}$ for the two midlatitude regions. So despite the slight discrepancy in the relative change in cloud cover and EIS for the North Atlantic region between winter and intermediate seasons, we find a reasonable agreement between the satellite estimates used here and WB06 by using MODIS cloud-conservative estimates of cloud cover and a 700-hPa cap on cloud-top pressure. Therefore, we are confident that we can use these datasets to explore this relationship in post-cold-frontal regions.

b. *Post-cold-frontal conditions in the North Atlantic and North Pacific regions*

In regions of weak subsidence, the strength of the inversion and cloud cover are related because the inversion controls the mixing at cloud top (KH93). Post-cold-frontal regions are dominated by subsidence and populated by low-level clouds, but it is not known how frequent or strong inversions might be and how much they can control cloud cover when large-scale dynamics influences the region. So using the two satellite datasets tested above and the two regions in the northern oceans,

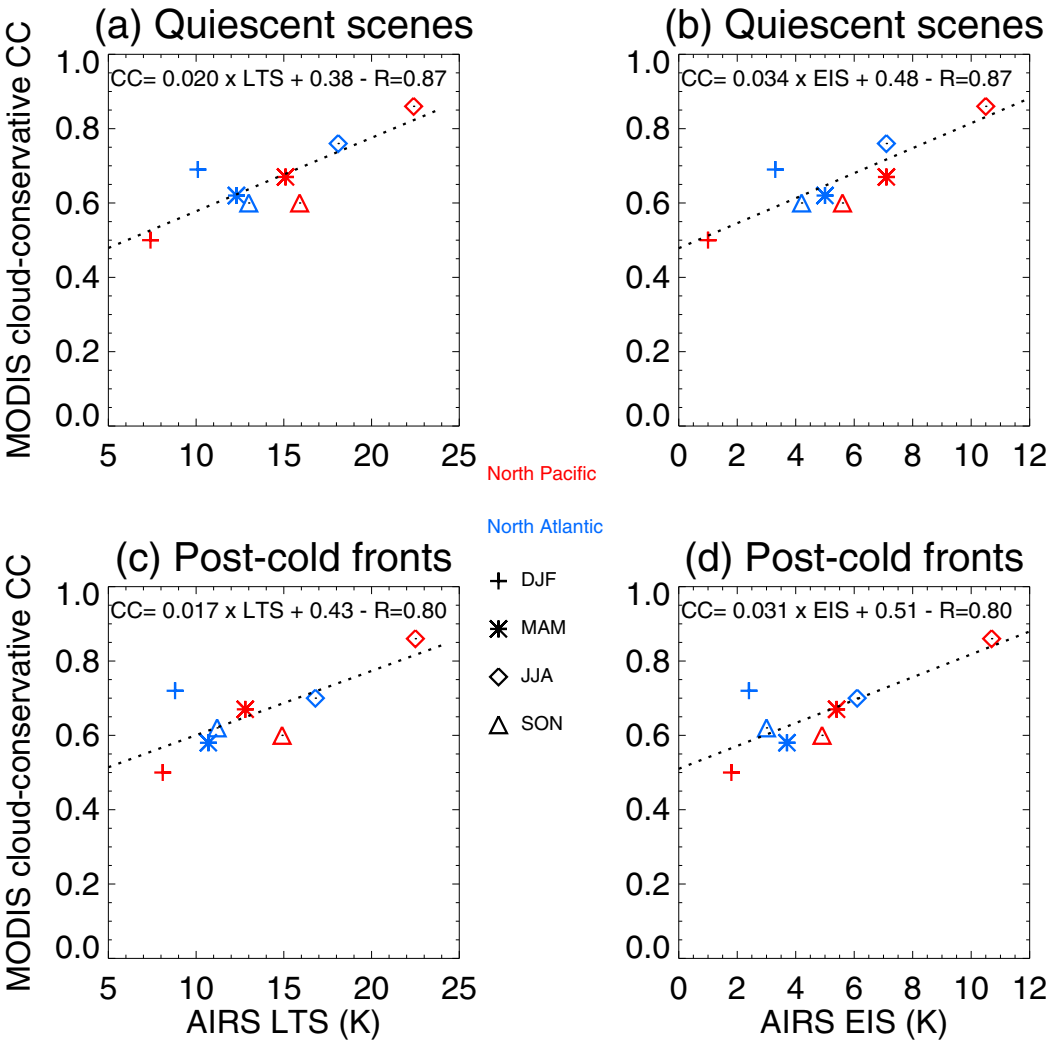

FIG. 2. MODIS seasonal average of cloud-conservative low-level cloud cover (CTP > 700 hPa) in the North Atlantic (50°–60°N, 35°–45°W) and North Pacific (40°–50°N, 170°–180°E) regions of KH93 as a function of AIRS estimates of (a),(c) LTS and (b),(d) EIS for (a),(b) all weakly subsiding and undisturbed (quiescent) AIRS data points and (c),(d) AIRS and MODIS data points in post-cold-frontal conditions. The dotted lines represent the result of a linear regression across all data points and their equations are given at the top of each panel.

we investigate how seasonal averages of cloud cover correlate with inversion strength in post-cold-frontal regions.

Once the cold front locations are found, we select data points of the two regions examined above that are acquired within ±3 h of the cold front detection and in the post-cold-frontal region within 1000 km west of the cold front. We require that these data points are at least 500 km away from the low pressure center of the parent cyclone to avoid contamination by the storm's occlusion. The number of data points with MODIS cloud-cover retrievals is 10%–15% of that available for section 3a. There is an intersect between the dataset of section 3a and this one because data points in post-cold-frontal conditions can experience subsidence rates in the 0.2–0.8 cm s^{-1} range.

Figures 2c,d show the relationship between seasonal averages of MODIS cloud-conservative cloud cover and AIRS LTS and EIS for both locations when a post-cold-frontal situation has been diagnosed. The seasonal averages of both cloud-cover definitions and inversion strength parameters are also available in Table 2. In effect, the AIRS LTS/EIS seasonal averages have now been calculated over dynamically active post-cold-frontal conditions with a wide range of subsidence strength. This said, we find that the ERA-Interim vertical velocity distribution for these data points still peaks in the 0.2–0.8 cm s^{-1} range (not shown). However, we

TABLE 2. As in Table 1, but for AIRS and MODIS seasonal averages of LTS, EIS, and cloud cover in the same two regions when post-cold-frontal conditions occur.

	AIRS		MODIS	
Season–region	LTS (K)	EIS (K)	Clear-conservative CC (%)	Cloud-conservative CC (%)
DJF-NA	8.8	2.4	86	72
MAM-NA	10.7	3.7	81	58
JJA-NA	16.8	6.1	84	70
SON-NA	11.2	3.0	83	62
DJF-NP	8.1	1.8	78	54
MAM-NP	12.8	5.4	81	61
JJA-NP	22.5	10.7	94	89
SON-NP	14.9	4.9	74	54

now include the data with much stronger or weaker subsidence as well.

Figures 2c,d reveal that despite changes in the seasonal averages for each location and all parameters, the overall relationship between cloud cover and both LTS and EIS is very similar to that found when constraining the subsidence strength. The linear regressions indicate a similar slope and the correlation coefficients are only slightly diminished. We tested whether this relationship was modified when we impose that both MODIS and AIRS simultaneously provide a retrieval. For this, we recalculated the seasonal mean cloud cover, LTS, and EIS for the two regions when coincidence was found between the two instruments in post-cold-frontal conditions. The condition was met for about a quarter of all the MODIS data points and caused the seasonal mean cloud cover to decrease by 1%–3%. By also removing instances when MODIS was not available (e.g., when high clouds are present) but AIRS was, we also find a slight decrease in LTS and EIS per season and region. However, a regression fit gave very similar slope and intercept as given in Figs. 2c,d ($CC = 0.018 \times LTS + 0.39$ and $CC = 0.032 \times EIS + 0.48$).

These results indicate that in the two northern midlatitude oceanic regions the inclusion of situations more dynamically active than intended by KH93 and WB06 does not alter the overall linearity of the relationship between cloud cover and LTS–EIS nor the slope and intercept of a linear regression. However, these results are limited to the two KH93 regions and possibly affected by the small sample size.

4. Relationship between cloud cover and EIS in a cold-front-centered frame of reference

To generalize the results obtained above, we no longer limit our analysis to the fixed locations used in KH93 and instead consider all post-cold-frontal regions over the oceans during the 2006/07 12-month period. For this, we use a cold front frame of reference and a compositing technique in which we average the MODIS and AIRS data points based on their position relative to the cold front. This allows us to investigate not only the relationship between cloud cover and inversion strength using seasonal averages obtained from multiple post-cold-frontal regions but also the same relationship within post-cold-frontal regions. We describe our methodology below.

a. Cold-front-centered compositing

The methodology presented here is illustrated in Fig. 3. For each extratropical cyclone–cold front pair, we collect MODIS low-level cloud cover and AIRS LTS and EIS, where the field of view of the instruments intersects a circular region of 25° radius (~2500 km at these latitudes) centered on the low pressure point within ±3 h (Fig. 3a). We then project the retrievals onto a stereographic grid centered on the low and with angular and radial resolution of 14.4° and 100 km, respectively (Fig. 3b).

A linear fit in latitude and longitude of the overall location of the cold front is calculated (the dotted line in Fig. 3b), and the intersection between this line and the latitude of the low pressure center is found. The stereo-gridded fields are then translated so that the new center of the stereo grid becomes this intersect. Next the stereo-gridded fields are rotated so the cold front direction is oriented north–south (Fig. 3c). For the Northern Hemisphere cold season (November to March), Fig. 4 shows where the cold fronts are located with respect to the low pressure centers (Fig. 4a) and then with respect to the center of rotation (Fig. 4b). Figure 4b verifies that in the new frame of reference the cold fronts are much closer together and are confined to a region ~200-km wide, with the bulk of the rotated fronts within 1000 km of the axis of rotation.

We define the post-cold-frontal zone as the region of the translated–rotated grid bounded by the latitude of the storm center for the poleward edge and the cold front to the east and extending westward and equatorward by

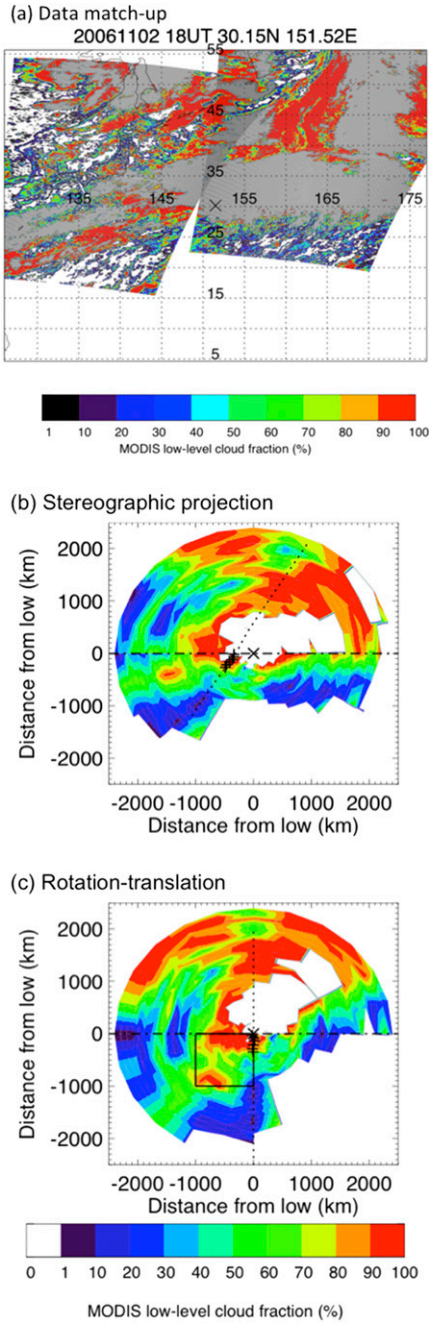

FIG. 3. Schematic of cold-front-centered compositing. Example for North Pacific cyclone centered on 30.15°N and 151.52°E on 1800 UTC 2 Nov 2006 of (a) matchup between the cyclone and five near-coincident MODIS granules showing low-level cloud cover (%, colors with clear or no data in white and clouds with CTP < 700 hPa in gray); (b) projection and averaging of MODIS clear-conservative cloud fraction onto a stereographic grid centered on the low pressure center, with the × symbol showing the location of the low pressure center, the + signs showing the cold front location, and the dotted line the best fit of the cold front general orientation (clear or no data and high clouds in white); (c) the MODIS cloud cover after rotation of the stereographic grid—the box marks the area selected for compositing, and the center of rotation is the intersect between the cold front orientation and the latitude of the low, marked with × (clear or no data and high clouds in white).

1000 km (Fig. 3c). In this idealized post-cold-frontal region, we composite cloud cover, LTS, and EIS for multiple cold fronts by averaging together these translated–rotated grids. Because of the translational shift and rotations described above, the low pressure centers and warm fronts for each cyclone are not superimposed for these composites. Because we want to ensure that there is as little contamination as possible in our composites from the area surrounding the low pressure center, before we translate and rotate the datasets we set the data values in the 500-km radius area centered on the low to their null values. However, it proved more difficult to remove data points close to the warm front in occluding situations, so there might still be some contamination from ascending regions.

The composites are constructed for four different subsets of our cold front database per hemisphere for December to February (DJF), March to May (MAM), June to August (JJA), and September to November (SON). By using seasonal composites, we can identify the most salient features of the post-cold-frontal sector. Our database includes cyclone centers between 30° and 60°N–S for November 2006 to October 2007. Cold fronts can be found between 20° and 60°N–S, and for each season and hemisphere, we have 800–1200 Northern Hemisphere (NH) cold fronts with collocated and coincident AIRS data and 1000–1600 with MODIS data. For Southern Hemisphere (SH) cold fronts, there are 1000–2000 with AIRS and 1200–2500 with MODIS data.

b. Results

Figure 5 shows the cold-front-centered composites of AIRS LTS and EIS for the four NH seasons. Figures 5a and 5c reveal a large contrast between winter and summer, respectively, with much lower LTS in winter. For all seasons except summer, there is a relative maximum in LTS in the region closest to the low pressure centers, where contamination by ascending regimes may occur more often (Figs. 5m–p show composites of the corresponding ERA-Interim 850-hPa vertical velocities and confirm the more ascending nature of this corner of the composites). The intermediate seasons show fairly consistent values of LTS spatially, but across all four seasons the area with the lowest LTS values moves with respect to the cold front. In contrast, for all seasons, the EIS relative minimum is found along the cold fronts and EIS tends to increase westward. Contrary to LTS, EIS values tend to decrease between winter and summer and are minimum in the fall. These seasonal variations illustrate the difference between LTS and EIS, with the latter taking into account the change in potential temperature along the moist adiabat, which tends to increase with surface air temperature (WB06, their Fig. 4).

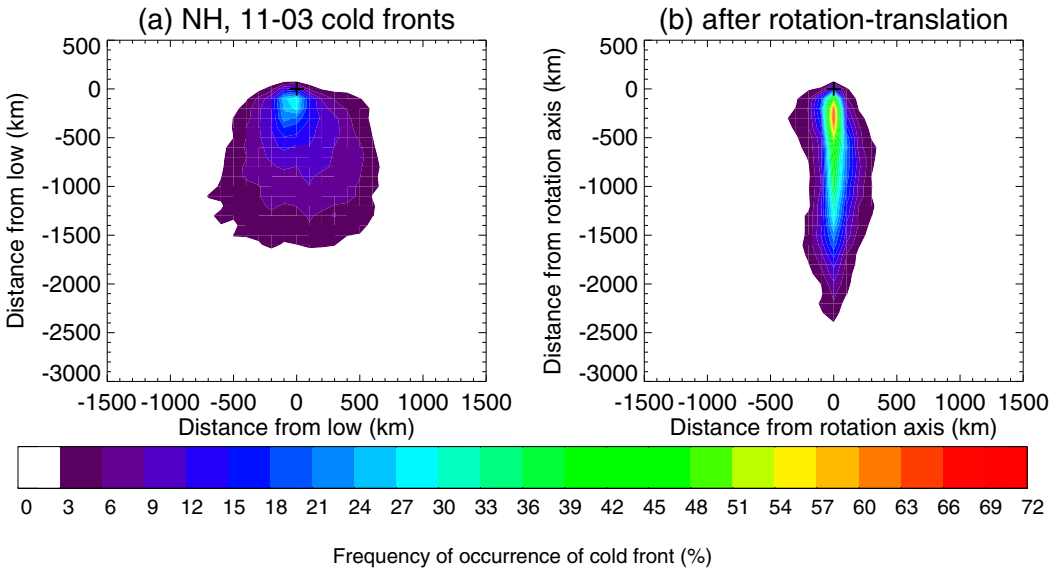

FIG. 4. Frequency of occurrence of cold frontal points location with respect to (a) the low pressure center and (b) the axis of rotation defined in Fig. 3.

This entails that as temperature increases, the inversion strength amounts to a smaller fraction of LTS. In agreement with WB06, we find that the seasonal variability of EIS differs from that of LTS mainly as a result of the influence of the variability in Γ_m^{850}, rather than the variability in the Z_{700} − LCL (not shown). This is also confirmed by the much larger correlation coefficient per season between EIS and Γ_m^{850} than between EIS and Z_{700} − LCL (not shown).

Figure 6 shows the post-cold-frontal composites of low-level cloud cover (CTP > 700 hPa) using the MODIS clear- and cloud-conservative cloud masks, as well as the difference between the two, for all NH seasons. As previously discussed, clear conservative cloud cover is by definition much greater than cloud conservative cloud cover. For both definitions, though, we find similar seasonal variations in cloud cover in the post-cold-frontal zone. There is a cloud-cover maximum close to the cold front where the influence of the low pressure center and warm fronts can be present (as mentioned earlier, the impact of the occlusion and corresponding ascending motions cannot be fully eliminated; cf. Figs. 5m–p). Cloud cover decreases westward and equatorward. The seasonal variations are more pronounced for cloud-conservative cloud cover and suggest a decrease in cloud cover from a maximum in winter to a minimum in fall. This is consistent with the seasonal change in EIS (Figs. 5e–h).

The difference between the two cloud-cover definitions, which we refer to as "the frequency of partly filled pixels," indirectly indicates whether clouds might be eroding in situations of weak inversion and large entrainment and so should also be related to the strength of the inversion—the larger the difference, the more "holes" might occur in the cloud cover. Another possibility is that it can indicate a change in cloud type from stratocumulus to cumulus. We also note that the value of this 5 km × 5 km parameter might change with scale. Figures 6i–l show that the frequency increases westward and equatorward of the region of the rotation axis. We find that its relative maximum per season increases between winter and fall. These results suggest that in winter, clouds are less broken and of larger cloud cover when present than in summer or fall. This is also consistent with the change in inversion strength as measured with EIS.

Based on Figs. 5 and 6, we find that the spatial distributions of LTS and cloud cover (from both definitions) have little correlation in the postfrontal region. Figures 5 and 6 also reveal differences in the seasonal variations of LTS and cloud cover; in summer LTS is the largest of all four seasons, but cloud cover is lower than in winter. Figure 7 shows scatterplots of post-cold-frontal cloud cover versus LTS with each point representing the average for each season for all data points found at the same 100 km × 100 km location in the 1000 km × 1000 km region defined with respect to the position of the low pressure center and cold front. For both definitions of cloud cover, we find a poor correlation between cloud cover and LTS when considering all data points (Figs. 7a–c), in part because cloud cover tends to decrease when LTS increases across seasons and within each composite.

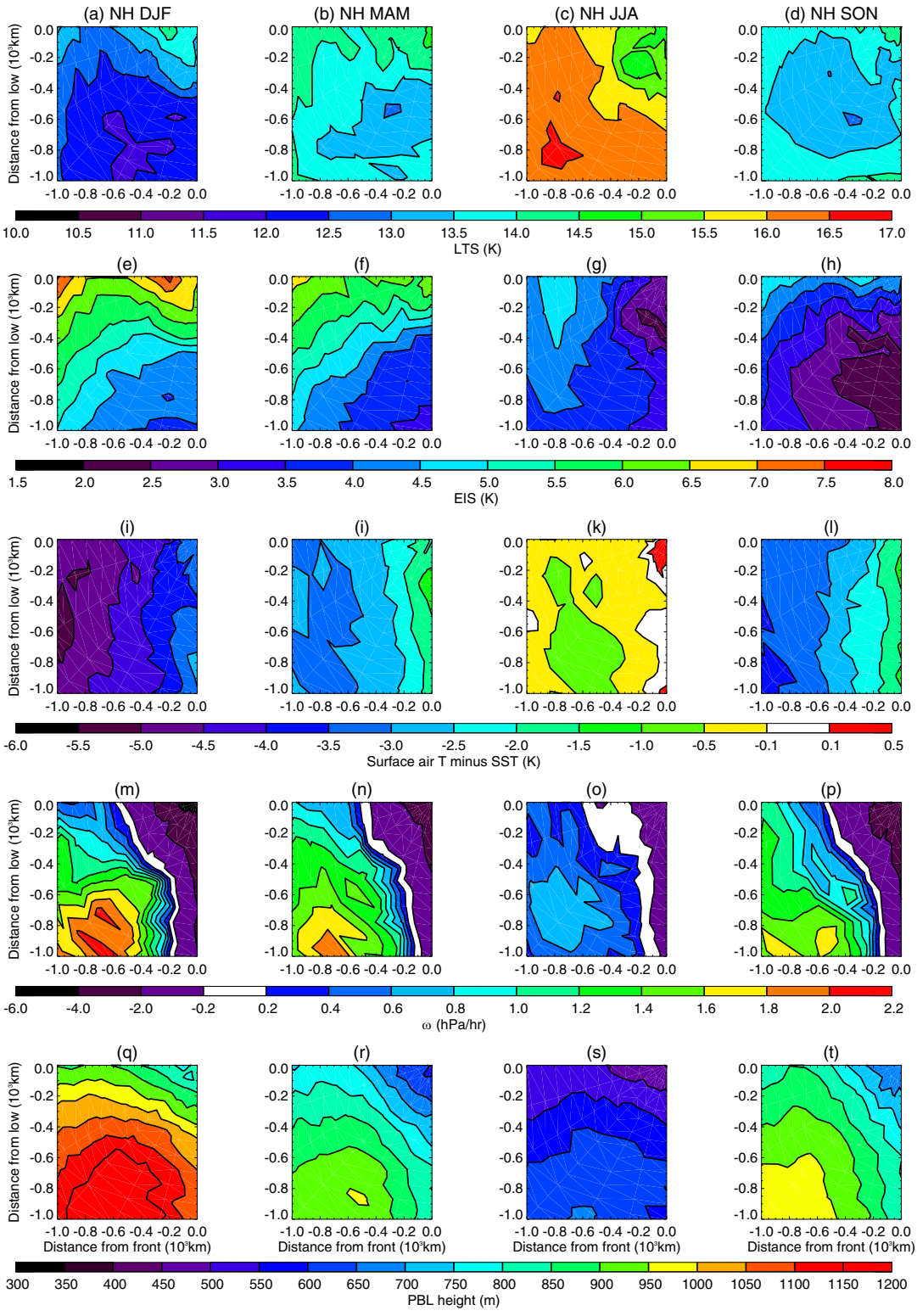

FIG. 5. Cold-front-centered composites of (a)–(d) AIRS LTS, (e)–(h) AIRS EIS, (i)–(l) difference between AIRS air and AMSR-E sea surface temperature, (m)–(p) ERA-Interim vertical velocity ω, and (q)–(t) ERA-Interim PBL height in Northern Hemisphere post-cold-frontal regions with the horizontal axis showing the distance to the cold front on the right and the vertical axis being the distance equatorward from the latitude of the low. The composites are for subsets (a),(e) DJF, (b),(f) MAM, (c),(g) JJA, and (d),(h) SON.

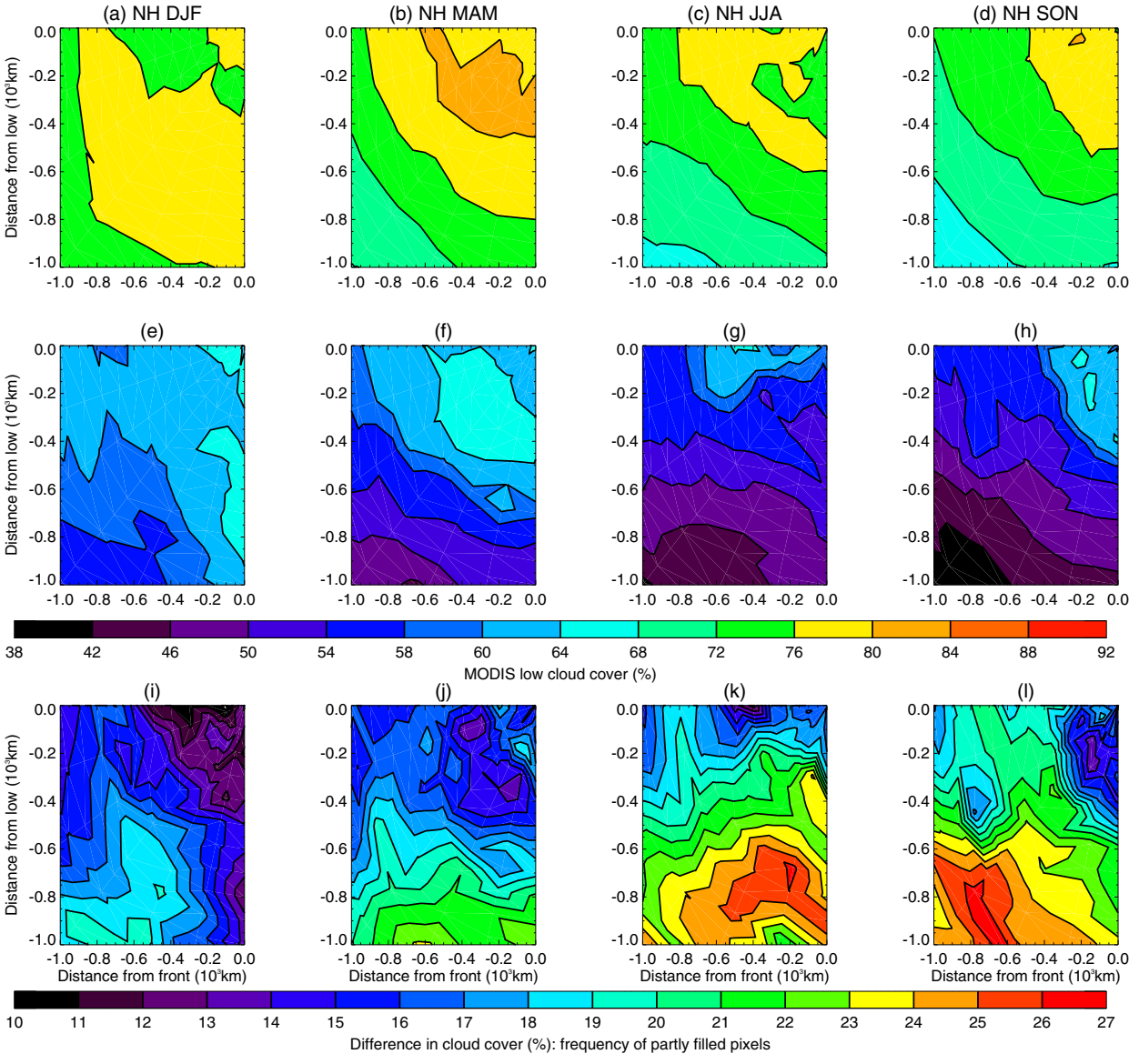

FIG. 6. Cold-front-centered composites of MODIS (a)–(d) clear-conservative cloud cover, (e)–(h) cloud-conservative cloud cover, and (i)–(l) the difference between the two for (left to right) NH DJF, MAM, JJA, and SON. The horizontal axis is the distance to the cold front on the right and the vertical axis is the distance equatorward from the latitude of the low.

However, Figs. 5 and 6 also suggest that despite their lack of clear spatial correlation for a given season, the seasonal variations of EIS and cloud cover are in agreement with what we expect: lower cloud cover when EIS is lower. In fact, the correlation between cloud-conservative cloud cover and EIS is fairly large (0.6) as shown in Fig. 8b and even larger (0.7) for the relation between the frequency of partly filled pixels and EIS (Fig. 8c). Although the scatter is quite large, there is a tendency for cloud cover to change linearly with EIS in the NH post-cold-frontal regions across the four seasons. However, for each individual season, the spatial correlation between cloud cover and EIS is weaker, especially in summer, and the slope of a least squares fit changes with season (Table 3).

For the Southern Hemisphere, Figs. 9 and 10 show the seasonal composites of LTS–EIS and cloud cover, respectively. Figure 9 reveals that the variations across seasons of LTS and EIS are in phase and increase between winter and summer. Overall, LTS values in the SH are lower than in the NH but the spatial variations per season are consistent. When we compare NH and SH EIS distributions we find that the largest differences between the hemispheres occur in winter and summer—much less so for the intermediate seasons.

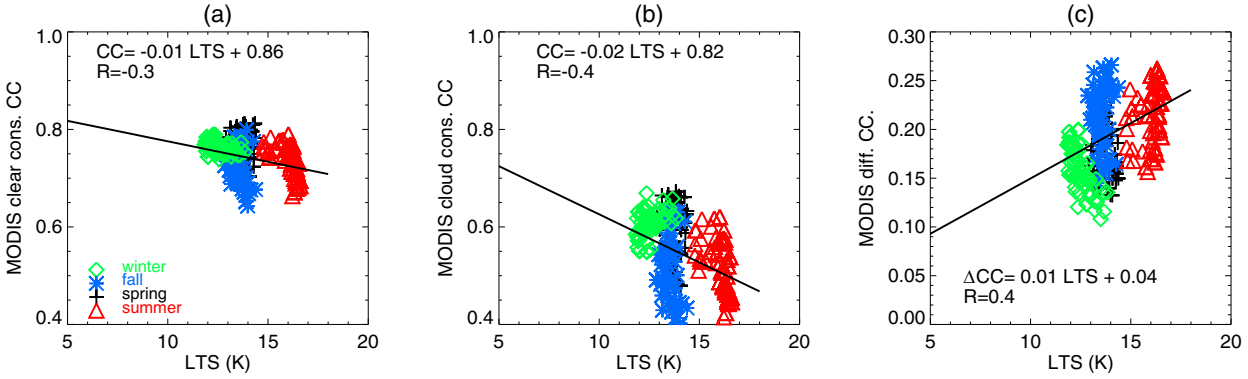

FIG. 7. Relationship between AIRS LTS and MODIS (a) clear-conservative cloud cover, (b) cloud-conservative cloud cover, and (c) difference between the two for NH winter (green), summer (red), fall (blue), and spring (black). The R values are the correlation coefficients for all data points and all seasons, and the equations and solid lines are the result of a linear regression performed on all data points for all seasons. Each data point represents the seasonal average in 100 km × 100 km grid cells that populate the region represented in the composites of Figs. 5, 6, 9, and 10.

Figure 10 reveals that SH cloud cover is lowest in the west-equatorward corner (i.e., farthest from the cyclone centers) for all seasons, and the minimum in cloud cover is lower in winter than summer. The frequency of partly filled pixels is largest in winter and lowest in summer, suggesting a larger frequency of occurrence of broken clouds in winter than summer. This result is consistent with the variations in both EIS and LTS, although we find again that the cloud cover and EIS–LTS do not display a one-to-one spatial match. This said, the scatterplots of cloud cover versus LTS (Fig. 11) reveal a much better correlation in SH than NH and the correlation is of the expected sign: both LTS and cloud-cover increase between winter and summer. Figure 11c shows a fairly good correlation of 0.7 between LTS and the frequency of partly filled pixels: the larger the LTS, the lower the frequency of occurrence of broken clouds.

Figure 12 shows the relationship between cloud cover and EIS for the Southern Hemisphere. For both definitions of cloud cover, the correlation coefficient for all data points across the four seasons is >0.5, with a larger value for the cloud-conservative cloud cover of 0.7. Furthermore, Table 3 shows that for each season independently the correlation between EIS and the cloud-conservative cloud cover is also fairly large (0.6 and above), especially in winter (R = 0.8). Figure 12c also shows a very good correspondence between EIS and the frequency of partly filled pixels.

Going back to the issue of allowing MODIS and AIRS retrievals in the composites regardless of their concomitant availability, we reproduced the same scatterplot and regression given in Figs. 7b, 8b, 11b, and 12b using only the coincident data. As found in section 3b for the WB06 regions, the biggest change is a reduction of MODIS mean cloud cover but also a slight decrease in the correlation and a change in the slopes of the regressions. This causes the linear fit and correlation coefficients between cloud-conservative cloud cover versus EIS to become CC = 0.024 × EIS + 0.38 (R = 0.4) for NH and for SH CC = 0.036 × EIS + 0.37 (R = 0.5). Thus,

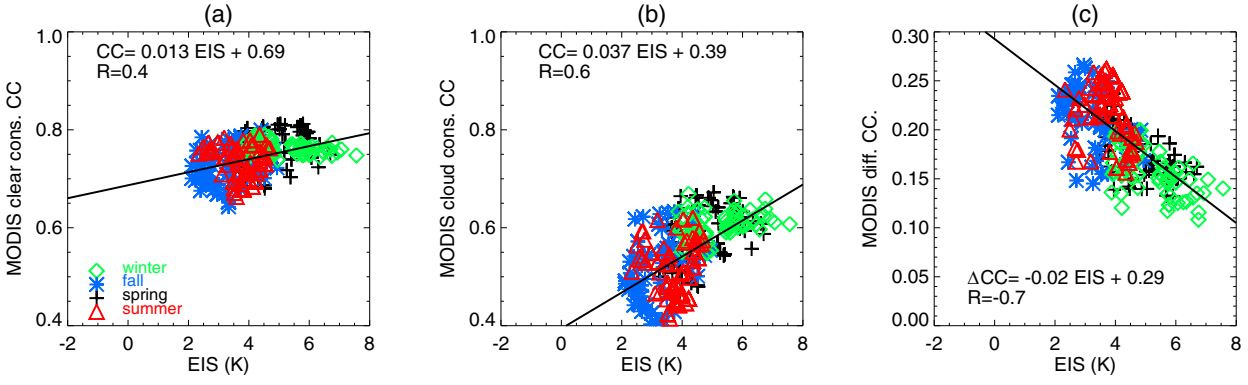

FIG. 8. As in Fig. 7, but for AIRS EIS instead of LTS.

TABLE 3. Correlation coefficient and slope (K^{-1}) for a linear regression between MODIS cloud-conservative cloud cover and AIRS EIS in NH and SH post-cold-frontal regions for all four seasons separately.

Hemisphere	Season	Correlation coefficient: CC vs EIS	Slope: CC vs EIS
NH	Winter	0.4	0.011
	Spring	0.5	0.032
	Summer	0.1	0.009
	Fall	0.3	0.031
SH	Winter	0.8	0.036
	Spring	0.6	0.044
	Summer	0.5	0.031
	Fall	0.7	0.059

the condition of coincidence creates a reduction in sample size that has an impact on the composites; however, we reach the same qualitative conclusions.

c. Discussion

Overall our results suggest that cloud cover and EIS are well correlated in post-cold-frontal regions, when considering regional and seasonal averages, in line with the results found by WB06 for quiescent conditions. This is somewhat surprising, given that the dynamic circulation in ETCs dominates the synoptic-scale patterns of clouds in these storms. However, we also find some issues, which are summarized here and then discussed in detail below:

1) The SH post-cold-frontal regions display a relationship between cloud cover and EIS much closer to WB06 results (large correlation, similar slope of a linear regression) than the NH regions. Moreover, the contrast between winter and summer cloud cover in the NH is opposite to what LTS variations would suggest.
2) The relationship between cloud cover and EIS is linear across seasons with a slope similar to WB06, but the correlation coefficients are smaller for the relationship per season in the post-cold-frontal regions, especially in the NH.

The SH results confirm that the measure of inversion strength proposed by WB06 is a good predictor of cloud cover in post-cold-frontal regions of SH storms, whether we consider the overall average per season for all available post-cold-frontal regions or in post-cold-frontal regions for each season separately. These results also suggest that despite the large-scale dynamical influence of the parent storm, local conditions and the boundary layer structure can still control cloud cover in these regions. The slope of $0.038\,K^{-1}$ for the cloud-conservative cloud cover versus EIS is close to the $0.03\,K^{-1}$ estimate of Yue et al. (2011), who also used satellite observations but included all regions (including subtropical) from KH93 and WB06 to obtain their estimate.

The results we obtained for the NH post-cold-frontal regions in each individual season are more difficult to interpret. The weaker correlation per season between cloud cover and EIS in NH (vs SH), especially during summer, could stem from two methodological problems: 1) there might be contamination in the MODIS and AIRS composites from pixels over land, and 2) despite the large number of cyclones per season the sample size might be too small.

To test the sensitivity to the first issue, we iteratively removed cyclones that were too close to the eastern coastlines of the continents by checking our results for larger and larger distances. This had no impact on the winter–summer contrast in EIS–cloud cover or on the scatter in Figs. 7 and 8. The second issue is more complicated to explore because of the data volume, but previous work of cloud-cover compositing had revealed little difference between 1 or 4 yr of data (Naud et al. 2013), and so we doubt that the impact of sample size can explain the winter–summer contrast.

Thus, the seasonal and hemispheric differences in the cloud cover–EIS relationship are most likely due to a combination of environmental factors. Myers and Norris (2015, and references therein) recap the factors that can have an impact on cloud cover in stratocumulus regions, such as the subsidence strength, the surface temperature, the horizontal cold air advection near the surface, and the free-tropospheric moisture. In an effort to approximate these large-scale parameters, here we use ERA-Interim 850-hPa vertical velocities ω and planetary boundary layer heights (PBLH), AIRS specific humidity at 850 hPa (q_{850}) and 700 hPa (q_{700}), and the difference (ΔT_{surf}) between AIRS surface air temperature and the Advanced Microwave Scanning Radiometer for Earth Observing System (AMSR-E; Kawanishi et al. 2003) sea surface temperature of the level 2 ocean products files (Wentz and Meissner 2004).

Because of the significant contrast between the two hemispheres, we first examine the influence of land in the Northern Hemisphere. The land in the NH produces greater air–sea temperature contrast in cold air outbreaks for NH winter coastal storms and virtually no contrast for summer storms (e.g., Fletcher et al. 2016a). Fletcher et al. (2016b) find that stronger cold air outbreaks exhibit larger cloud cover than weak ones. Therefore, we calculate as a measure of the occurrence of cold air outbreaks the difference ΔT_{surf} between AIRS air temperature and AMSR-E sea surface temperature. The composites of ΔT_{surf} for all four seasons in NH are shown in Figs. 5i–l and indeed exhibit a large contrast between winter and summer.

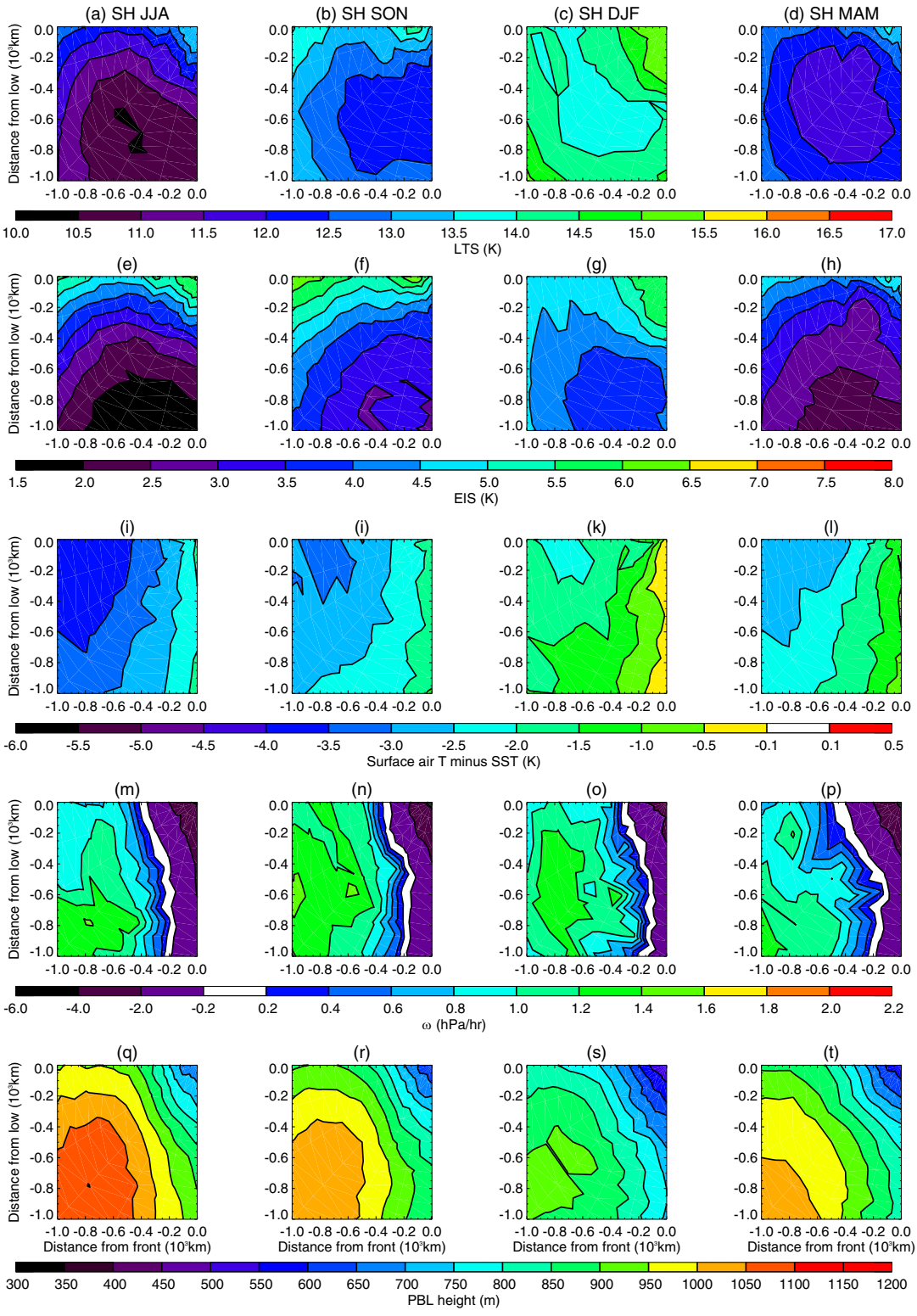

FIG. 9. As in Fig. 5, but for the Southern Hemisphere. The composites are ordered to align boreal and austral seasons so the first column shows JJA.

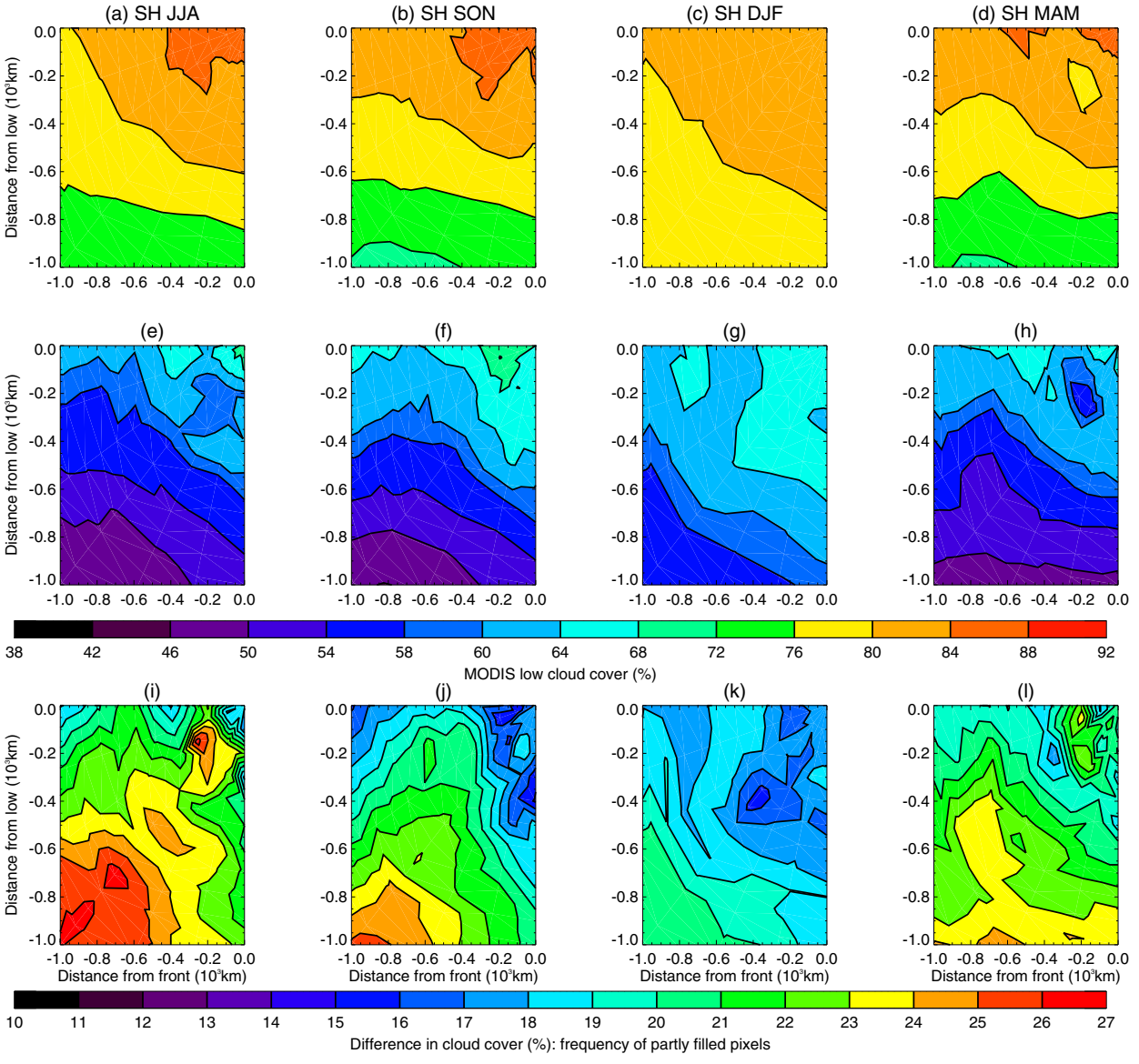

FIG. 10. As in Fig. 6, but for the Southern Hemisphere. The composites are ordered to align boreal and austral seasons so the first column shows JJA.

In contrast, the seasonal variations in ΔT_{surf} are weaker in the SH (Figs. 9i–l). Cold air outbreak conditions are thus found more often in NH winter post-cold-frontal regions than in other seasons or in SH in all seasons (consistent with Fletcher et al. 2016a). This said, in the post-cold-frontal regions, the spatial correlation between ΔT_{surf} and cloud cover is weak in both hemispheres and all seasons. Moreover, if the relationship between cloud cover and EIS is weakened by the occurrence of cold air outbreak conditions, then NH summer post-cold-frontal regions should exhibit a better correlation between cloud cover and EIS than in winter, which we do not see.

Next, we composited ω, PBLH, q_{850}, and q_{700}. We explored their correlation with cloud cover per season and across seasons but also their cross correlation, including with LTS, EIS, and ΔT_{surf}. Table 4 summarizes the cross-correlation coefficients between these seven parameters, when calculated per season and hemisphere and for all seasons and both hemisphere. For convenience, we only show summer and winter values. We find that both q_{850} and q_{700} are highly correlated with one another, regardless of season, and with ΔT_{surf} except for NH summer. Consistent with this, the specific humidity also has a weak relationship with cloud cover as discussed above for ΔT_{surf} (not shown). Table 4 also reveals

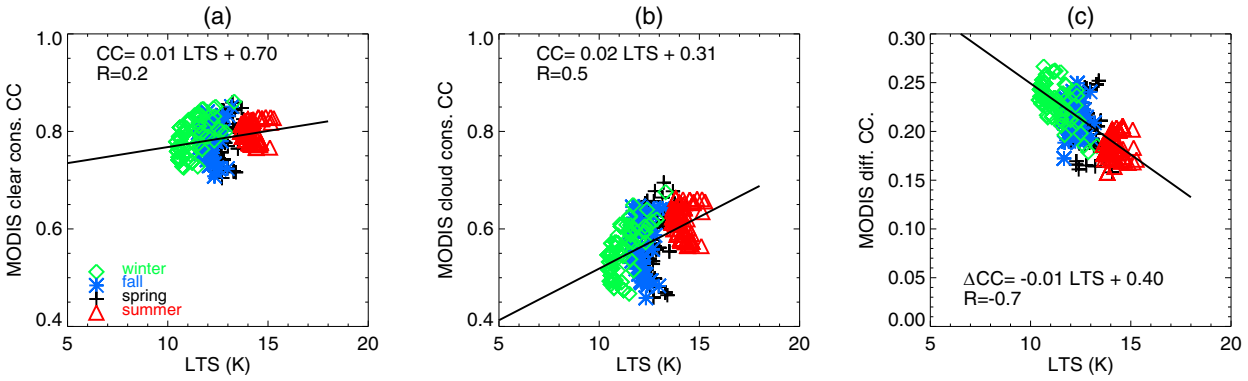

FIG. 11. As in Fig. 7, but for the Southern Hemisphere.

differences in the cross-correlation coefficient between subsets. For example, LTS and EIS are highly correlated for both hemispheres in winter but less so in summer and weakly when all seasons are considered. Overall, with the exception of q_{850} and q_{700}, which are always strongly correlated, there are large variations in the degree of correlation or anticorrelation between all seven parameters across seasons. Based on these results, we examine composites of ω and PBLH but choose not to examine the specific humidity composites because of their fairly large correlation with ΔT_{surf} in most seasons.

Figures 5m–p show composites of ERA-Interim vertical velocities for each season in the NH post-cold-frontal regions, while Figs. 9i–l show the same for the SH regions. For each season, the spatial distribution of the vertical velocity seems to correlate better with cloud cover in the region of subsidence than does EIS; as subsidence increases, cloud cover decreases. However, this relationship is not seen across seasons; that is, stronger values of vertical velocity in winter than in summer are at odds with greater cloud cover in winter than summer in the NH. This suggests that locally in the post-cold-frontal regions, the subsidence rates might have an impact on cloud cover but that the seasonal variations are better related to EIS. This was verified by making a similar scatterplot as Fig. 7 (Fig. 13); although there is a strong correlation for each season individually between cloud cover and vertical velocity, this correlation is weak when all data points for all four seasons are included in the regression.

The composites of ERA-Interim boundary layer heights are shown in Figs. 5q–t for the NH and Figs. 9q–t for the SH. We note a clear correlation between subsidence strength and boundary layer height; as the cold air mass moves across relatively warmer water in the post-cold-frontal regions, the contrast between the two causes instability, which leads to a deeper boundary layer. This causes a transition from stratocumulus to cumulus clouds, which would explain the decrease in cloud cover in the post-cold-frontal regions as the boundary layer becomes deeper. But as we noted earlier when discussing the relationship between subsidence strength and cloud cover, although there is a strong spatial anticorrelation between the boundary layer heights and cloud cover, the relationship weakens across seasons.

Next, we give in Table 5 the percentage of variance explained obtained with a multiple linear regression of the MODIS cloud-conservative cloud cover on all the parameters examined here in post-cold-frontal regions

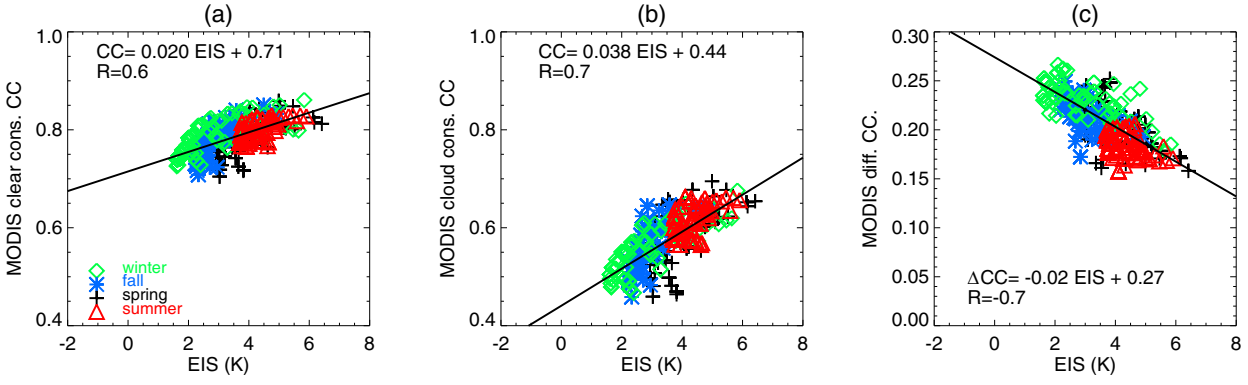

FIG. 12. As in Fig. 8, but for the Southern Hemisphere.

TABLE 4. Cross-correlation coefficients between seven parameters for NH winter (NH summer), SH winter (SH summer), and all seasons and both hemispheres cold frontal regions. Values for SH winter and SH summer are given in italics, and those for all seasons and both hemispheres are given in bold. The parameters are defined in the text.

Parameters	EIS	ω	ΔT_{surf}	PBLH	q_{850}	q_{700}
LTS	0.90 (0.72)	−0.66 (0.67)	−0.01 (−0.51)	−0.89 (0.64)	−0.08 (−0.20)	0.05 (−0.07)
	0.94 (0.66)	*−0.36 (−0.54)*	*−0.29 (0.28)*	*−0.54 (−0.48)*	*−0.29 (0.34)*	*−0.01 (0.51)*
	0.36	**−0.11**	**0.64**	**−0.79**	**0.79**	**0.84**
EIS	1	−0.41 (0.63)	−0.35 (−0.43)	−0.85 (0.04)	−0.45 (−0.78)	−0.34 (−0.64)
		−0.30 (−0.44)	*−0.39 (−0.18)*	*−0.54 (−0.61)*	*−0.41 (−0.24)*	*−0.14 (−0.17)*
		−0.06	**−0.25**	**−0.13**	**−0.21**	**−0.14**
ω	—	1	−0.62 (−0.67)	0.77 (0.54)	−0.57 (−0.39)	−0.65 (−0.29)
			−0.70 (−0.67)	*0.90 (0.88)*	*−0.67 (−0.62)*	*−0.83 (−0.54)*
			−0.33	**0.50**	**−0.26**	**−0.20**
ΔT_{surf}	—	—	1	−0.11 (−0.53)	0.95 (0.23)	0.92 (0.17)
				−0.53 (−0.50)	*0.97 (0.90)*	*0.93 (0.79)*
				−0.81	**0.81**	**0.81**
PBLH	—	—	—	1	−0.01 (0.42)	−0.11 (0.43)
					−0.52 (−0.44)	*−0.71 (−0.30)*
					−0.83	**−0.84**
q_{850}	—	—	—	—	1	0.97 (0.91)
						0.95 (0.91)
						0.99

for each season individually and both hemispheres. We start with the seven parameters (LTS, EIS, ω, ΔT_{surf}, PBLH, q_{850}, and q_{700}), and then we redo the experiment when removing each parameter separately. For simplicity we only give the percentages of variance explained for winter and summer. For winter in both hemispheres, the largest impact on the variance explained is found when LTS is removed, and EIS has the second largest impact. In the NH summer, EIS has the largest impact and LTS comes second, while in the SH summer, LTS again dominates and PBLH has a larger impact than EIS. These results suggest that for a specific season and hemisphere, the variation in the moist adiabat is not such a large factor, except for NH summer. The SH summer percentages suggest that in this season and hemisphere PBLH has an impact on cloud cover. However, as shown in Table 4, there are strong cross correlations between the parameters that change with hemisphere and season, so it is difficult to establish with certainty that a given parameter is the sole influence on cloud cover. So to establish the respective impact of each of these parameters on cloud cover, we also calculated the correlation coefficient between cloud cover and each parameter individually. These results are given in Table 6. It suggests that in NH winter, ω displays the largest correlation (in absolute value) with cloud cover, while in NH summer it is PBLH. In SH winter, EIS dominates, while in SH summer, again PBLH displays the largest correlation with cloud cover in absolute value. Table 6 also reveals that some of these coefficients are close to one another, presumably because of the larger cross correlations shown in Table 4. Therefore, for a given season, within post-cold-frontal regions, cloud cover can be influenced by more than one environmental factor.

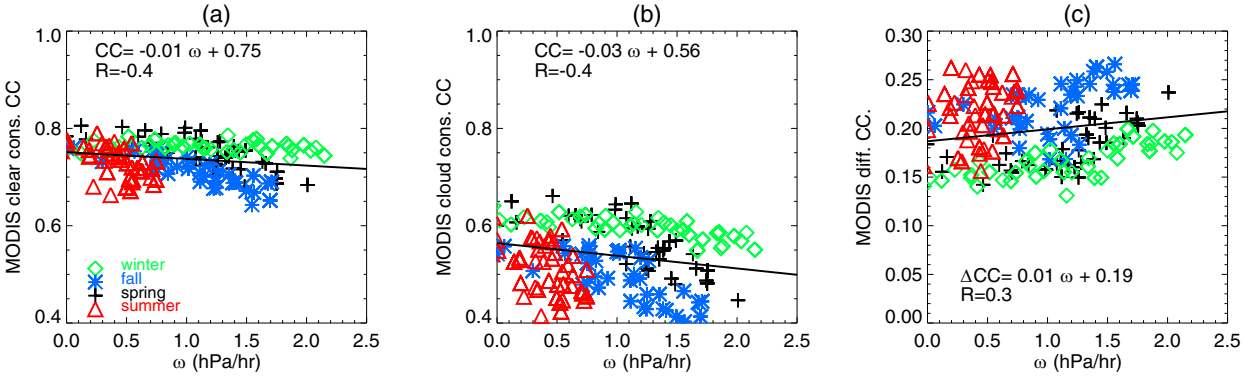

FIG. 13. As in Fig. 7, but for ERA-Interim 850-hPa vertical velocity ω instead of LTS.

TABLE 5. Percentage (%) of the variance explained when performing, in post-cold-frontal regions, a multivariate regression of MODIS cloud-conservative cloud cover on seven parameters and then on six parameters (the first column indicates which parameter is removed from the first multiple regression) for NH winter, NH summer, SH winter, SH summer, and all four seasons and both hemispheres. The parameters are defined in the text.

	NH winter	NH summer	SH winter	SH summer	NH and SH, all seasons
All parameters	80.15	87.81	91.55	83.15	71.26
No LTS	70.37	81.97	84.11	79.83	64.05
No EIS	73.41	81.40	88.24	81.64	59.76
No ω	79.16	87.39	91.52	83.15	71.26
No ΔT_{surf}	78.47	87.57	91.49	83.01	63.14
No PBLH	79.97	86.90	91.38	80.88	70.89
No q_{850}	79.69	85.33	91.54	81.93	70.96
No q_{700}	79.79	85.93	91.52	81.83	71.11

To generalize these results, we redid the same analysis using all data points for both hemispheres and all four seasons, as shown in the last column of Table 5. When all seasons are included, we find that in fact EIS has a larger impact than LTS and dominates over all parameters. In addition, Table 6 shows that for this larger dataset, EIS is better correlated with cloud cover than any of the other large-scale parameters examined here. This is consistent with the main result of WB06: EIS is a better predictor of cloud cover across different regions and seasons. Interestingly, the impact of ΔT_{surf} is slightly larger than the impact of LTS, presumably indicative of the role of cold air outbreaks for modulating cloud cover.

Finally, we emphasize that although in post-cold-frontal regions cloud cover is strongly influenced by the dynamics of the cold air outbreak conditions, the relationship between cloud cover and EIS is the only one we find that is linear across seasons for both hemispheres.

5. Conclusions

Combining two methods for cold front detection by Hewson (1998) and Simmonds et al. (2012), and using a cold-front-centered compositing method, we examined the relationship between cloud cover and boundary layer stability in post-cold-frontal regions where low-level clouds are present two-thirds of the time. Boundary layer stability is characterized using the measure proposed by Klein and Hartmann (1993), called lower-tropospheric stability (LTS), and the more recent measure proposed by Wood and Bretherton (2006), called the estimated inversion strength (EIS). For this, we use satellite observations: the two MODIS cloud-cover retrievals—one that is clear conservative while the other is cloud-conservative. Boundary layer stability measures LTS and EIS are obtained using AIRS profiles of temperature and surface air temperature.

After ensuring that these two satellite datasets give a linear relationship between the seasonal and regional mean of cloud cover and inversion strength with a similar slope as in KH93 and WB06 for weak subsidence in fixed regions in the midlatitudes, we then considered the more actively dynamic conditions in post-cold-frontal regions. Overall, we found a good correlation between cloud cover and both measures of inversion in post-cold-frontal conditions at two locations in the northern oceans.

Then we explored the same relationship for one year of post-cold-frontal regions in the midlatitude oceans of seasonal averages and found that cloud cover was better correlated with EIS than LTS in both hemispheres across seasons. As explained in WB06, as temperature increases, so does the vertical gradient of potential temperature, causing the fraction of LTS corresponding to the inversion strength to be smaller than at colder

TABLE 6. Correlation coefficient between cloud cover and seven parameters for post-cold-frontal regions in NH winter and summer and SH winter and summer, as well as for all seasons and both hemispheres.

	NH winter	NH summer	SH winter	SH summer	NH and SH, all seasons
LTS	0.45	−0.54	0.61	−0.07	−0.14
EIS	0.36	0.09	0.78	0.49	0.53
ω_{850}	−0.79	−0.41	−0.49	−0.43	−0.35
ΔT_{surf}	0.54	0.40	−0.05	0.01	−0.11
PBLH	−0.67	−0.88	−0.73	−0.68	−0.05
q_{850}	0.43	−0.48	−0.07	−0.10	−0.37
q_{700}	0.46	−0.55	0.13	−0.33	−0.35

temperatures for the same LTS. This is particularly true for the NH summer post-cold-frontal regions, which exhibit relatively larger LTS but relatively lower cloud cover than in winter. In contrast, EIS in summer is overall lower than in winter in NH post-cold-frontal regions.

The good correlation between cloud cover and EIS in dynamically active conditions, in particular in the southern oceans where the impact of landmasses is limited, suggests that the boundary layer structure and its relation with cloud cover is relatively independent of the large-scale conditions typically found in post-cold-frontal regions.

However, in post-cold-frontal regions, the seasonal means of cloud cover and EIS are better spatially correlated in the southern than Northern Hemisphere. They are also better correlated across seasons than spatially within seasons. We found that the strength of the subsidence rate and boundary layer depth also impact the cloud cover. In the NH, the large land–sea contrast, which is virtually absent in the SH, favors the occurrence of strong conditions of cold air outbreak in the winter and intermediate seasons, causing a strong impact of the surface temperature contrast on cloud cover. However, a multivariable regression analysis of cloud cover on a series of large-scale parameters performed for all seasons and both hemispheres emphasized the dominant role of EIS for cloud cover in post-cold-frontal regions, while LTS has a greater role when considering a specific season and hemisphere.

The Northern Hemisphere results call for a more detailed analysis of the local atmospheric profiles as a function of season in post-cold-frontal regions and would necessitate profiles at a higher resolution than currently available with AIRS. This will have to be part of a separate study. Going back to the issues in GCMs that were evoked in the introduction, these results can be useful as an observational constraint for model evaluation. By applying the method presented here to model output, one could assess the skills of both the boundary layer scheme and cloud scheme in these regions of extratropical cyclones.

Acknowledgments. The collection 5.1 MYD06 files were obtained from the level 1 Atmosphere Archive and Distribution System at the Goddard Space Flight Center. The AIRS-AMSU L2 Standard Product files and MERRA output files were obtained from the Goddard Earth Sciences Data and Information Services Center. The AMSR-E L2B ocean products were obtained from the National Snow and Ice Data Center. The Warren et al. (1988) cloud atlas climatology is available online (http://www.atmos.washington.edu/CloudMap/). ERA-Interim files are available through the European Centre for Medium-Range Weather Forecasts website. The MCMS dataset, documentation, and algorithm are available online (http://gcss-dime.giss.nasa.gov/mcms/). We thank Mike Bauer for the ERA-Interim-based dataset. CMN was funded by NASA's Science of *Terra* and *Aqua* Grant NNX11AH22G, NOAA's MAPP program Grant NA15OAR4310094, and NASA *CloudSat* Science Team Recompete Grant NNX13AQ33G. JFB was partially funded by NOAA's MAPP program Grant NA15OAR4310094. ADD was funded by a *CloudSat*/*CALIPSO* Science Team RTOP. We thank three anonymous reviewers and the editor who helped significantly improve this manuscript.

REFERENCES

Ackerman, S. A., R. E. Holz, R. Frey, E. W. Eloranta, B. C. Maddux, and M. McGill, 2008: Cloud detection with MODIS. Part II: Validation. *J. Atmos. Oceanic Technol.*, **25**, 1073–1086, doi:10.1175/2007JTECHA1053.1.

Bauer, M. P., and A. D. Del Genio, 2006: Composite analysis of winter cyclones in a GCM: Influence on climatological humidity. *J. Climate*, **19**, 1652–1672, doi:10.1175/JCLI3690.1.

——, G. Tselioudis, and W. B. Rossow, 2016: A new climatology for investigating storm influences in and on the extratropics. *J. Appl. Meteor. Climatol.*, **55**, 1287–1303, doi:10.1175/JAMC-D-15-0245.1.

Bodas-Salcedo, A., and Coauthors, 2014: Origins of the solar radiation biases over the Southern Ocean in CFMIP2 models. *J. Climate*, **27**, 41–56, doi:10.1175/JCLI-D-13-00169.1.

Bolton, D., 1980: The computation of equivalent potential temperature. *Mon. Wea. Rev.*, **108**, 1046–1053, doi:10.1175/1520-0493(1980)108<1046:TCOEPT>2.0.CO;2.

Chahine, M. T., and Coauthors, 2006: AIRS: Improving weather forecasting and providing new data on greenhouse gases. *Bull. Amer. Meteor. Soc.*, **87**, 911–926, doi:10.1175/BAMS-87-7-911.

Dee, D. P., and Coauthors, 2011: The ERA-Interim reanalysis: Configuration and performance of the data assimilation systems. *Quart. J. Roy. Meteor. Soc.*, **137**, 553–597, doi:10.1002/qj.828.

Field, P. R., A. Bodas-Salcedo, and M. E. Brooks, 2011: Using model analysis and satellite data to assess cloud and precipitation in midlatitude cyclones. *Quart. J. Roy. Meteor. Soc.*, **137**, 1501–1515, doi:10.1002/qj.858.

Fletcher, J., S. Mason, and C. Jakob, 2016a: The climatology, meteorology, and boundary layer structure of marine cold air outbreaks in both hemispheres. *J. Climate*, **29**, 1999–2014, doi:10.1175/JCLI-D-15-0268.1.

——, ——, and ——, 2016b: A climatology of clouds in marine cold air outbreaks in both hemispheres. *J. Climate*, **29**, 6677–6692, doi:10.1175/JCLI-D-15-0783.1.

Garay, M. J., S. O. de Szoeke, and C. M. Moroney, 2008: Comparison of marine stratocumulus cloud top heights in the southeastern Pacific retrieved from satellites with coincident ship-based observations. *J. Geophys. Res.*, **113**, D18204, doi:10.1029/2008JD009975.

Govekar, P. D., C. Jakob, and J. Catto, 2014: The relationship between clouds and dynamics in Southern Hemisphere extratropical cyclones in the real world and a climate model. *J. Geophys. Res. Atmos.*, **119**, 6609–6628, doi:10.1002/2013JD020699.

Hewson, T. D., 1998: Objective fronts. *Meteor. Appl.*, **5**, 37–65, doi:10.1017/S1350482798000553.

Holz, E. E., S. A. Ackerman, F. W. Nagle, R. Frey, S. Dutcher, R. E. Kuehn, M. A. Vaughan, and B. Baum, 2008: Global Moderate Resolution Imaging Spectroradiometer (MODIS) cloud detection and height evaluation using CALIOP. *J. Geophys. Res.*, **113**, D00A19, doi:10.1029/2008JD009837.

Hwang, Y.-T., and D. M. W. Frierson, 2013: Link between the double-intertropical convergence zone problem and cloud biases over the Southern Ocean. *Proc. Natl. Acad. Sci. USA*, **110**, 4935–4940, doi:10.1073/pnas.1213302110.

Kawanishi, T., and Coauthors, 2003: The Advanced Microwave Scanning Radiometer for the Earth Observing System (AMSR-E), NASDA's contribution to the EOS for global energy and water cycle studies. *IEEE Trans. Geosci. Remote Sens.*, **41**, 184–194, doi:10.1109/TGRS.2002.808331.

Klein, S. A., and D. L. Hartmann, 1993: The seasonal cycle of low stratiform clouds. *J. Climate*, **6**, 1587–1606, doi:10.1175/1520-0442(1993)006<1587:TSCOLS>2.0.CO;2.

Köhler, M., M. Ahlgrimm, and A. Beljaars, 2011: Unified treatment of dry convective and stratocumulus-topped boundary layers in the ECMWF model. *Quart. J. Roy. Meteor. Soc.*, **137**, 43–57, doi:10.1002/qj.713.

Lau, N.-C., and M. W. Crane, 1997: Comparing satellite and surface observations of cloud patterns in synoptic-scale circulation systems. *Mon. Wea. Rev.*, **125**, 3172–3189, doi:10.1175/1520-0493(1997)125<3172:CSASOO>2.0.CO;2.

Menzel, W. P., and Coauthors, 2008: MODIS global cloud-top pressure and amount estimation: Algorithm description and results. *J. Appl. Meteor. Climatol.*, **47**, 1175–1198, doi:10.1175/2007JAMC1705.1.

Myers, T. A., and J. R. Norris, 2015: On the relationships between subtropical clouds and meteorology in observations and CMIP3 and CMIP5 models. *J. Climate*, **28**, 2945–2967, doi:10.1175/JCLI-D-14-00475.1.

Naud, C. M., A. D. Del Genio, M. Bauer, and W. Kovari, 2010: Cloud vertical distribution across warm and cold fronts in *CloudSat–CALIPSO* data and a general circulation model. *J. Climate*, **23**, 3397–3415, doi:10.1175/2010JCLI3282.1.

——, J. F. Booth, D. J. Posselt, and S. C. van den Heever, 2013: Multiple satellite observations of cloud cover in extratropical cyclones. *J. Geophys. Res. Atmos.*, **118**, 9982–9996, doi:10.1002/jgrd.50718.

——, ——, and A. D. Del Genio, 2014: Evaluation of ERA-Interim and MERRA cloudiness in the Southern Ocean. *J. Climate*, **27**, 2109–2124, doi:10.1175/JCLI-D-13-00432.1.

——, D. J. Posselt, and S. C. van den Heever, 2015: A *CloudSat–CALIPSO* view of cloud and precipitation properties across cold fronts over the global oceans. *J. Climate*, **28**, 6743–6762, doi:10.1175/JCLI-D-15-0052.1.

Norris, J. R., and S. F. Iacobellis, 2005: North Pacific cloud feedbacks inferred from synoptic-scale dynamic and thermodynamic relationships. *J. Climate*, **18**, 4862–4878, doi:10.1175/JCLI3558.1.

Platnick, S., M. D. King, S. A. Ackerman, W. P. Menzel, B. A. Baum, J. C. Riedi, and R. A. Frey, 2003: The MODIS cloud products: Algorithms and examples from Terra. *IEEE Trans. Geosci. Remote Sens.*, **41**, 459–473, doi:10.1109/TGRS.2002.808301.

Rasch, P. J., and J. E. Kristjánnson, 1998: A comparison of the CCM3 model climate using diagnosed and predicted condensate parameterizations. *J. Climate*, **11**, 1587–1614, doi:10.1175/1520-0442(1998)011<1587:ACOTCM>2.0.CO;2.

Rienecker, M. M., and Coauthors, 2011: MERRA: NASA's Modern-Era Retrospective Analysis for Research and Applications. *J. Climate*, **24**, 3624–3648, doi:10.1175/JCLI-D-11-00015.1.

Salomonson, V. V., W. L. Barnes, P. W. Maymon, H. E. Montgomery, and H. Ostrow, 1989: MODIS: Advanced facility instrument for studies of the earth as a system. *IEEE Trans. Geosci. Remote Sens.*, **27**, 145–153, doi:10.1109/36.20292.

Schemm, S., I. Rudeva, and I. Simmonds, 2015: Extratropical fronts in the lower troposphere—Global perspectives obtained from two automated methods. *Quart. J. Roy. Meteor. Soc.*, **141**, 1686–1698, doi:10.1002/qj.2471.

Simmonds, I., K. Keay, and J. A. T. Bye, 2012: Identification and climatology of Southern Hemisphere mobile fronts in a modern reanalysis. *J. Climate*, **25**, 1945–1962, doi:10.1175/JCLI-D-11-00100.1.

Susskind, J., C. D. Barnet, and J. M. Blaisdell, 2003: Retrieval of atmospheric and surface parameters from AIRS/AMSU/HSB data in the presence of clouds. *IEEE Trans. Geosci. Remote Sens.*, **41**, 390–409, doi:10.1109/TGRS.2002.808236.

Trenberth, K. E., and J. Fasullo, 2010: Simulation of present-day and twenty-first-century energy budgets of the southern oceans. *J. Climate*, **23**, 440–454, doi:10.1175/2009JCLI3152.1.

Tselioudis, G., and C. Jakob, 2002: Evaluation of midlatitude cloud properties in a weather and a climate model: Dependence on dynamic regime and spatial resolution. *J. Geophys. Res.*, **107**, 4781, doi:10.1029/2002JD002259.

Warren, S. G., C. J. Hahn, J. London, R. M. Chervin, and R. L. Jenne, 1988: Global distribution of total cloud cover and cloud type amounts over the ocean. NCAR Tech. Note TN-317+STR, 42 pp.

Wentz, F., and T. Meissner, 2004: AMSR-E/Aqua L2B global swath ocean products derived from Wentz algorithm V002, 2006–2009. National Snow and Ice Data Center, Boulder, CO, digital media.

Wood, R., and C. S. Bretherton, 2006: On the relationship between stratiform low cloud cover and lower-tropospheric stability. *J. Climate*, **19**, 6425–6432, doi:10.1175/JCLI3988.1.

Yue, Q., B. H. Kahn, E. J. Fetzer, and J. Teixeira, 2011: Relationship between marine boundary layer clouds and lower tropospheric stability observed by AIRS, CloudSat, and CALIOP. *J. Geophys. Res.*, **116**, D18212, doi:10.1029/2011JD016136.